A Robust Dual-Loop Current Control Method With a Delay-Compensation Control Link for *LCL*-Type Shunt Active Power Filters

Lei Yang and Jiaqiang Yang, *Member, IEEE*

***Abstract*—This paper is focused on a dual-loop current control method (grid current loop and fundamental current loop) for digitally controlled *LCL*-type shunt active power filters (APFs). Normally, a proportional-resonant (PR) unit is used as the fundamental current controller, where the proportional part of PR unit actually serves as the proportional feedback of inverter-side current and provides a certain degree of damping for *LCL* resonance. However, its valid damping region is only up to one-sixth of the sampling frequency (f_s/6), which leads to less robustness to the grid impedance. To address this issue, a delay-compensation control link is proposed in this paper to replace the proportional part of the PR fundamental current controller and widen the effective damping region. As a result, the system robustness is improved without adding extra sensors or introducing an extra active damping loop. Theoretical analysis proves that it can obtain a wider damping region of (0, f_s/4). Moreover, a systematic controller parameter design criterion is studied. In particular, a numerical optimization algorithm is developed to optimize damping property, and a design method based on root locus plot and Bode diagram is presented to enhance harmonic compensation accuracy. Finally, experimental results implemented on a 30 kVA APF prototype have validated the feasibility of the proposed current controller and parameter design criterion.**

***Index Terms*—Active power filter (APF), delay-compensation control link, dual-loop current control, robustness.**

I. Introduction

THE harmonic pollution caused by nonlinear loads, rectifiers, switching power supplies, and other grid-connected power converters has rapidly increased. Power quality has therefore emerged as a popular research area in the field of distributed power generation systems based on renewable energy, such as wind and solar energy [1], [2]. Active power filters (APFs) are an effective way of solving grid harmonic pollution [3], [4].

For shunt APFs, an *L* filter or an *LCL* filter is used at the output to filter the pulsed voltages and reduce the switching harmonics [5]. Compared with the conventional *L* filter, the *LCL* filter is preferred for its better high-frequency harmonics attenuation ability. However, a resonance hazard is introduced by

Manuscript received April 7, 2018; revised July 1, 2018; accepted August 6, 2018. Date of publication August 16, 2018; date of current version May 2, 2019. This work was supported by the National Natural Science Foundation of China under Grant 51777191. Recommended for publication by Associate Editor H.-P. Nee. *(Corresponding author: Jiaqiang Yang.)*

The authors are with the College of Electrical Engineering, Zhejiang University, Hangzhou 310027, China (e-mail:

sampling instant to reduce the signal delay time and widen the damping region. However, careful design must be devoted to avoid signal aliasing and switching noises with this sampling technique. Another research direction is to insert a compensator into the active damping loop. In [26] and [27], different compensators are carefully designed to extend the damping region and improve the robustness to grid impedance. Besides, an above-Nyquist-frequency *LCL*-filter resonance has been explored in recent works [28], [29]. Tang *et al*. [28] achieve a very cost-effective *LCL* filter design by setting the resonance frequency higher than the Nyquist frequency, and Harnefors *et al*. [29] further present the input admittance model of voltage source inverters above the Nyquist frequency. This *LCL* filter design is more suitable for the grid-connected converters, whose dominant switching harmonics may appear at double the switching frequency. In this paper, a common two-level shunt APF is studied with the symmetry regular sampled PWM adopted, and the resonance frequency is placed less than $f_s/2$ to ensure the effective attenuation of switching harmonics.

To improve upon [24]–[27], we here investigate a dual-loop current control method for digitally controlled *LCL*-type shunt APFs, and find that the proportional part of the PR fundamental current controller actually serves as the proportional inverter-side current feedback and provides a certain degree of damping for *LCL* resonance. However, its valid damping region is only up to one-sixth of the sampling frequency ($f_s/6$) due to the system delays [23]–[27], and the control system is less robust to the grid impedance. Based on this issue, this paper proposes a delay-compensation control link to replace the proportional part of the PR fundamental controller and widen the damping region. Theoretical analysis proves that the control system can obtain a wider damping region of $(0,\ f_s/4)$ and improve the robustness, without adding extra sensors or introducing an extra active-damping loop. Moreover, a systematic controller parameter design criterion is studied. In particular, a numerical optimization algorithm is developed to optimize damping property, and a design method based on root locus plot and Bode diagram is presented to enhance harmonic compensation accuracy. The rest of this paper is organized as follows. Section II introduces the structure and models of dual-loop current control method. In Section III, considering that the proportional part of fundamental current controller actually serves as the proportional feedback of inverter-side current, the corresponding stability conditions are discussed. Section IV proposes a delay-compensation control link instead of the proportional part, and theoretically proves that the system can obtain a wider damping region of $(0,\ f_s/4)$. In Section V, a systematic parameter design criterion is developed to obtain satisfactory performances. Experimental results are presented in Section VI to verify the proposed current control and parameter design criterion. Finally, a conclusion is drawn in Section VII.

II. Model of the *LCL*-Type Three-Phase Shunt APF With Dual-Loop Current Control Method

Fig. 1 illustrates the general diagram of an *LCL*-type three-phase shunt APF with dual-loop current control method. As

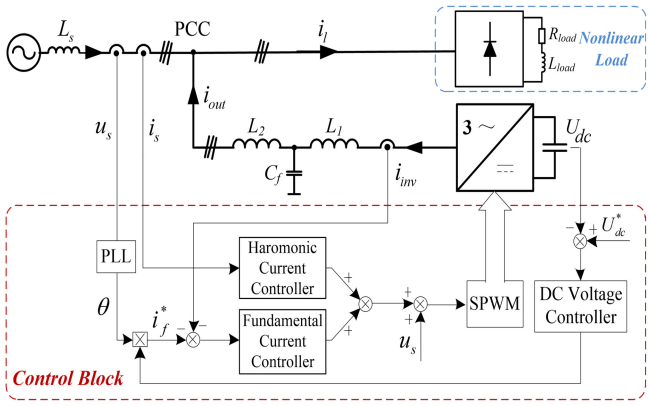

Fig. 1. Diagram of an *LCL*-type three-phase shunt APF with dual-loop current control method.

shown, the shunt APF is comprised of a two-level voltage source inverter with dccapacitors and an *LCL*-type output filter. L_1 is the inverter-side filter inductor, L_2 is the grid-side filter inductor, and C_f is the filter capacitor. A three-phase diode rectifier with resistive and inductive load is adopted as a harmonic source. The power grid at the point of common coupling (PCC) is represented as a voltage source in series with the grid impedance. u_s is the grid voltage at PCC. Generally, the grid impedance contains inductance and resistance [30]. Since grid resistance and parasitic resistances of inductors all provide a certain degree of damping for *LCL*-filter resonance, they are ignored here to draw the worst case. Thus, a pure inductance L_s is used to denote the grid impedance, and it can be regarded as part of L_2.

In Fig. 1, it is found that a harmonic current controller and a fundamental current controller are in parallel to constitute dual loops of APF control system (grid current loop and fundamental current loop), and the grid current and the inverter-side current are adopted as their feedback variables. For grid current loop, it aims to eliminate the harmonic components of grid current i_s. The reference of grid harmonic currents is set to 0. Considering that the harmonic current controller only regulates harmonic signals, i_s is directly fed to the harmonic controller without harmonic extraction. For fundamental current loop, it aims to track the fundamental current reference i_f^* and maintain dc-side voltage $U_{\rm dc}$ constant. i_f^* is generated by the output of dcvoltage controller and phase angle of u_s. Since the inverter-side current $i_{\rm inv}$ actually contains the fundamental component of APF output current $i_{\rm out}$, $i_{\rm inv}$ is directly fed to the fundamental controller and compared with i_f^*. Note that no extra sensors or no extra active damping loop are contained in this control structure.

Based on Fig. 1, Fig. 2(a) gives the *s*-domain model of the *LCL*-type shunt APF with dual-loop current control method in the stationary $\alpha\beta$-frame. $-i_{\rm sh}^* = 0$ is the reference of grid harmonic currents. *PI* is the dc voltage controller. $G_{\rm ch}(s)$ and $G_{\rm cf}(s)$ are the harmonic current controller and the fundamental current controller, respectively. $1/T_s$ represents the sampler and T_s is the sampling period. $K_{\rm PWM}$ is the gain of the PWM inverter, and $K_{\rm PWM} \approx 1$ here. The computation and PWM delays are contained in the current control loops. $G_d(s) = e^{-sTs}$ is the computation delay of one sampling

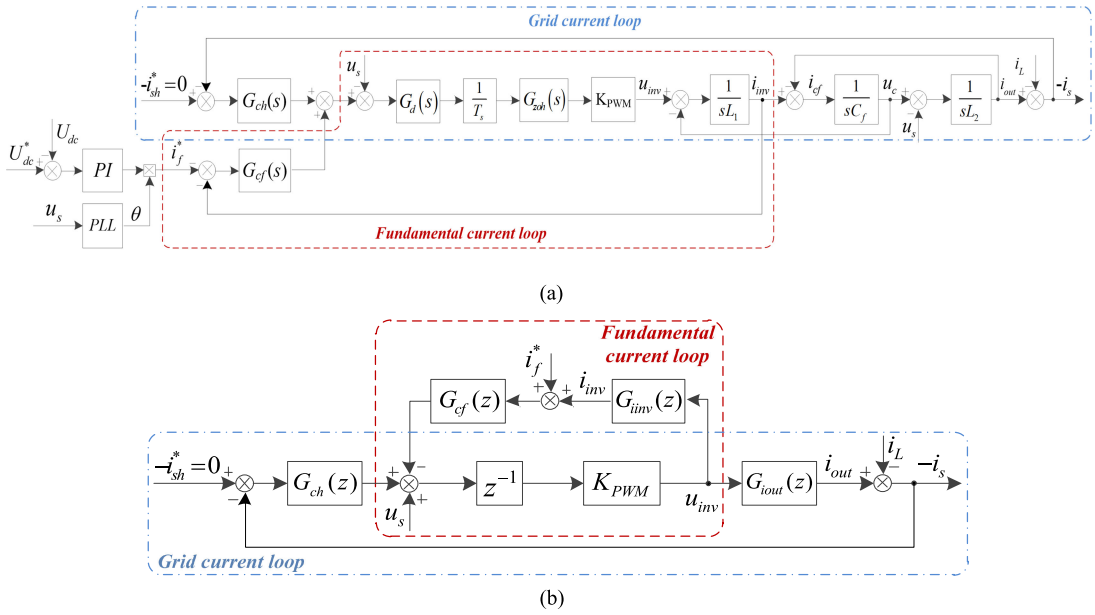

Fig. 2. Models of the *LCL*-type shunt APF with dual-loop current control method. (a) *s*-domain model. (b) *z*-domain model.

period, and $G_{\text{zoh}}(s) = (1-e^{-sT_s})/s \approx T_s e^{-0.5sT_s}$ is the transfer function of the zero-order hold (ZOH), which is an inherent property of PWM inverters.

According to Fig. 2(a), $G_{i\text{out}}(s)$ is the transfer function from the inverter voltage $u_{\text{inv}}(s)$ to the APF output current $i_{\text{out}}(s)$, which can be derived as

$$G_{i\text{out}}(s) = \frac{i_{\text{out}}(s)}{u_{\text{inv}}(s)} = \frac{1}{L_1 L_2 C_f s\left(s^2+\omega_r^2\right)} \tag{1}$$

where $\omega_r = 2\pi f_r$ is the resonance angular frequency of the *LCL* filter. Given the effect of grid impedance on the *LCL*-filter resonance frequency, ω_r can be expressed as

$$\omega_r = \sqrt{\frac{L_1+L_2+L_s}{L_1(L_2+L_s)C_f}}. \tag{2}$$

$G_{i\text{inv}}(s)$ is the transfer function from the inverter voltage $u_{\text{inv}}(s)$ to the inverter-side current $i_{\text{inv}}(s)$, which can be derived as

$$G_{i\text{inv}}(s) = \frac{i_{\text{inv}}(s)}{u_{\text{inv}}(s)} = \frac{L_2 C_f s^2+1}{L_1 L_2 C_f s\left(s^2+\omega_r^2\right)}. \tag{3}$$

Fig. 2(b) gives the *z*-domain model of the dual-loop current control method. The dc-side voltage control loop is ignored here, because it is usually designed to be a slow control loop and will not interact with the inner current control as long as a proper control bandwidth is chosen [31]. In Fig. 2(b), $G_{i\text{out}}(z)$ and $G_{i\text{inv}}(z)$ are the *z*-domain transfer functions of $G_{i\text{out}}(s)$ and $G_{i\text{inv}}(s)$. By applying the ZOH transformation to (1) and (3), $G_{i\text{out}}(z)$ and $G_{i\text{inv}}(z)$ can be derived as

$$\begin{aligned} G_{i\text{out}}(z) &= Z\left[G_{\text{zoh}}(s)\,G_{i\text{out}}(s)\right] \\ &= \frac{\omega_r T_s(z^2-2z\cos\omega_r T_s+1)-\sin\omega_r T_s(z-1)^2}{(L_1+L_2)\omega_r(z-1)(z^2-2z\cos\omega_r T_s+1)} \end{aligned} \tag{4}$$

$$\begin{aligned} G_{i\text{inv}}(z) &= Z\left[G_{\text{zoh}}(s)\,G_{i\text{inv}}(s)\right] \\ &= \frac{\omega_r T_s(z^2-2z\cos\omega_r T_s+1)+\frac{L_2}{L_1}\sin\omega_r T_s(z-1)^2}{(L_1+L_2)\omega_r(z-1)(z^2-2z\cos\omega_r T_s+1)}. \end{aligned} \tag{5}$$

In order to accurately describe the features of the digitally controlled APF system, the analysis is implemented in the *z*-domain. Besides, the symmetry regular sampled PWM method is adopted in this paper, i.e., the sampling frequency f_s is equal to the switching frequency f_{sw}. Table I lists the system parameters of the *LCL*-type three-phase shunt APF.

III. Stability Analysis With the Proportional Inverter-Side Current Feedback

In Fig. 2(b), a PR unit is normally adopted as the fundamental current controller $G_{\text{cf}}(z)$. In this case, the proportional part of the PR fundamental current controller actually serves as the proportional feedback of inverter-side current and provides a certain degree of damping for *LCL* resonance. Therefore, it remains necessary to present the stability analysis with the proportional inverter-side current feedback in this section. The resonant part of the PR fundamental controller is ignored, because it makes very limited effects far from the fundamental resonant frequency [26], [31]. Assuming that $G_{\text{cf}}(z) = K_{\text{pf}}$, the open-loop transfer function of grid current loop $T_p(z)$ can be derived from Fig. 2(b) as (6) shown at the bottom of the next page, where the

TABLE I
SYSTEM PARAMETERS OF THE *LCL*-TYPE THREE-PHASE SHUNT APF

Parameter	I	II
Grid impedance L_s	0	280 μH
Inverter-side inductor L_1	100 μH	
Grid-side inductor L_2	50 μH	
Filter capacitor C_f	80 μF	
Resonance frequency f_r	3.08 kHz	2.03 kHz
DC-side voltage U_{dc}	780 V	
Grid voltage U_s	220 V (RMS), 50 Hz	
Sampling frequency f_s	15 kHz	
Switching frequency f_{sw}	15 kHz	
Diode rectifier load R_{load} / L_{load}	20 Ω / 1 mH	

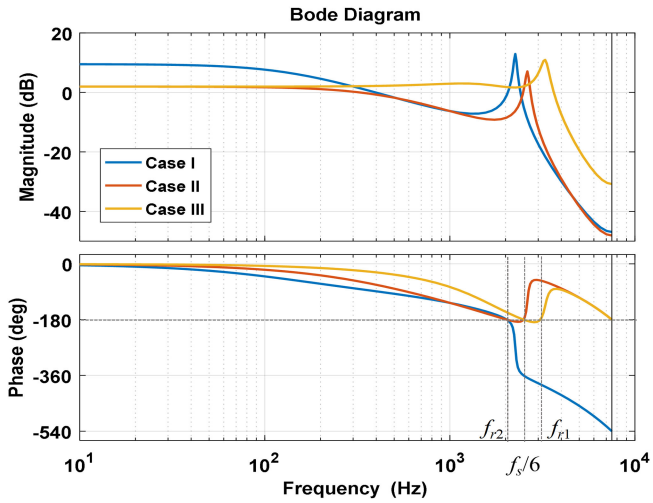

Fig. 3. Bode diagrams of $T_p(z)$ in three cases with $G_{\rm ch}(z) = 1\,\Omega$.

fundamental current loop is considered as an inner loop of grid current loop, and $K_{\rm pf}$ is the proportional gain of the fundamental current controller.

In order to ensure that no open-loop unstable poles exist in $T_p(z)$, the judging criterion for $K_{\rm pf}$ is derived in Appendix A as

$$0 < K_{\rm pf} < \min\left(K', K'', K'''\right) \text{ and } f_r \in \left(0, \frac{f_s}{6}\right) \tag{7}$$

where K', K'', K''' are defined as (8) shown at the bottom of this page.

From (7), it can be seen that only when $f_r < f_s/6$ and $0 < K_{\rm pf} < \min(K', K'', K''')$, no open-loop unstable poles will occur in $T_p(z)$. When $f_r > f_s/6$ or $K_{\rm pf} > \min(K', K'', K''')$, a pair of open-loop unstable poles will occur. Accordingly, three cases are divided to further illustrate the system stability as follows:

Case I: $f_r < f_s/6$ and $0 < K_{\rm pf} < \min(K', K'', K''')$.
Case II: $f_r < f_s/6$ and $K_{\rm pf} > \min(K', K'', K''')$.
Case III: $f_r > f_s/6$ and $K_{\rm pf} > 0$.

In Case I and Case II, the parameters in Table I are adopted with the inherent resonance frequency $f_{r2} = 2.03\,\text{kHz}$. Under this set of system parameters, a range which meets the judging criterion (7) is calculated as $0 < K_{\rm pf} < 0.636\,\Omega$. Hence, $K_{\rm pf} = 0.3\,\Omega$ is chosen for Case I, while $K_{\rm pf} = 0.8\,\Omega$ is chosen for Case II. In Case III, the parameters are adopted with the resonance frequency $f_{r1} = 3.08\,\text{kHz}$ and $\min(K', K'', K''') < 0$. No $K_{\rm pf}$ exists to meet (7), and $K_{\rm pf} = 0.8\,\Omega$ is chosen in this case. Accordingly, Fig. 3 shows the Bode diagrams of $T_p(z)$ in three cases, where $G_{\rm ch}(z) = 1\,\Omega$ for simplicity.

$$T_p(z) = G_{\rm ch}(z)K_{\rm pwm} \cdot \frac{\omega_r T_s(z^2 - 2z\cos\omega_r T_s + 1) - \sin\omega_r T_s(z-1)^2}{(L_1+L_2)\omega_r z(z-1)(z^2 - 2z\cos\omega_r T_s + 1) + K_{\rm pwm}K_{\rm pf}\left[\omega_r T_s(z^2 - 2z\cos\omega_r T_s + 1) + \frac{L_2}{L_1}\sin\omega_r T_s(z-1)^2\right]} \tag{6}$$

$$\begin{cases} K' \triangleq \dfrac{(L_1+L_2)\omega_r(1+\cos\omega_r T_s)}{K_{\rm pwm}\omega_r T_s(1+\cos\omega_r T_s) + 2K_{\rm pwm}\frac{L_2}{L_1}\sin\omega_r T_s} \\ \quad = \dfrac{(L_1+L_2)\omega_r}{K_{\rm pwm}\omega_r T_s + K_{\rm pwm}\frac{L_2}{L_1}\frac{2\sin\omega_r T_s}{1+\cos\omega_r T_s}} \\ K'' \triangleq \dfrac{(L_1+L_2)\omega_r T_s - 4(L_1+L_2)\frac{L_2}{L_1}\frac{\sin\omega_r T_s(1-2\cos\omega_r T_s)}{(1+\cos\omega_r T_s)^2}}{K_{\rm pwm}\omega_r {T_s}^2 + 4K_{\rm pwm}T_s\frac{L_2}{L_1}\tan 0.5\omega_r T_s + 4K_{\rm pwm}\frac{1}{\omega_r}\left(\frac{L_2}{L_1}\right)^2\tan^2 0.5\omega_r T_s} \\ K''' \triangleq \dfrac{(L_1+L_2)\omega_r(1-2\cos\omega_r T_s)}{K_{\rm pwm}\omega_r T_s(1-2\cos\omega_r T_s) - K_{\rm pwm}\frac{L_2}{L_1}\sin\omega_r T_s} \\ \quad = \dfrac{(L_1+L_2)\omega_r}{K_{\rm pwm}\omega_r T_s - K_{\rm pwm}\frac{L_2}{L_1}\frac{\sin\omega_r T_s}{(1-2\cos\omega_r T_s)}} \end{cases} \tag{8}$$

As seen from Fig. 3, the $-180°$ crossing of $T_p(z)$ might take place at f_r or $f_s/6$. In Case I, the $-180°$ crossing only takes place at f_r, while in Case II and Case III, the 180° crossing takes place at both f_r and $f_s/6$. Thus, the values of $T_p(z)$ at f_r and $f_s/6$ are concerned, and they can be derived from (6) as

$$T_p\left(z = e^{j\omega_r T_s}\right) = -\frac{K_{\rm ph} L_1}{K_{\rm pf} L_2} \tag{9}$$

$$T_p\left(z = e^{j\frac{\pi}{3}}\right) = \frac{K_{\rm ph}}{K_{\rm pf} - K'''} \cdot \frac{\omega_r T_s\,(1 - 2\cos\omega_r T_s) + \sin\omega_r T_s}{\omega_r T_s\,(1 - 2\cos\omega_r T_s) - \frac{L_2}{L_1}\sin\omega_r T_s} \tag{10}$$

where $K_{\rm ph}$ is the proportional gain of the harmonic current controller $G_{\rm ch}(z)$. In fact, $G_{\rm ch}(z)$ might contain multiple resonant controller units, but it can be reduced to a proportional gain at the $-180°$ crossover frequency [25], [31].

As mentioned above, the open-loop poles and frequency responses of the system are explored. Then, the stability analysis can be implemented. According to the Nyquist stability criterion [25], [32], the stability conditions with the proportional inverter-side current feedback are summarized as follows:

Case I [$f_r < f_s/6$, $0 < K_{pf} < min(K', K'', K''')$]: No open-loop unstable poles exist, and the phase plot of $T_p(z)$ crosses over $-180°$ only at f_r in the direction of phase falling. Hence, as long as the gain of T_p(z) at f_r is less than 0 dB, i.e., $|T_p(z = e^{j\omega r T s})| < 1$, the system will be stable. Accordingly, the corresponding stability condition can be derived from (9) as

$$0 < K_{\rm ph} < \frac{K_{\rm pf} L_2}{L_1}. \tag{11}$$

Case II [$f_r < f_s/6$, $K_{pf} > min(K', K'', K''')$]: A pair of open-loop unstable poles exists. The phase plot of $T_p(z)$ crosses over $-180°$ at f_r in the direction of phase falling, and at $f_s/6$ in the direction of phase rising. Therefore, to make the system stable, the gain of $T_p(z)$ at f_r must be less than 0 dB, and the gain of $T_p(z)$ at $f_s/6$ must be greater than 0 dB, i.e., $|T_p(z = e^{j\omega r T s})| < 1$ and $|T_p(z = e^{j\pi/3})| > 1$. Accordingly, the corresponding stability condition is derived from (9) and (10) as

$$\left|\left(K_{\rm pf} - K'''\right) \cdot \frac{\omega_r T_s\,(1 - 2\cos\omega_r T_s) - \frac{L_2}{L_1}\sin\omega_r T_s}{\omega_r T_s\,(1 - 2\cos\omega_r T_s) + \sin\omega_r T_s}\right| < K_{\rm ph} < \frac{K_{\rm pf} L_2}{L_1}. \tag{12}$$

Case III ($f_s/6 < f_r < f_s/2$, $K_{pf} > 0$): A pair of open-loop unstable poles exists. The phase plot of $T_p(z)$ crosses over $-180°$ at $f_s/6$ in the direction of phase falling, and at f_r in the direction of phase rising. Opposite to Case II, the gain of $T_p(z)$ at $f_s/6$ is required to be less than 0 dB, and the gain of $T_p(z)$ at f_r is required to be greater than 0 dB, i.e., $|T_p(z = e^{j\pi/3})| < 1$ and $|T_p(z = e^{j\omega r T s})| > 1$. Hence, the corresponding stability condition can be derived as

$$\frac{K_{\rm pf} L_2}{L_1} < K_{\rm ph} < \left|\left(K_{\rm pf} - K'''\right) \cdot \frac{\omega_r T_s\,(1 - 2\cos\omega_r T_s) - \frac{L_2}{L_1}\sin\omega_r T_s}{\omega_r T_s\,(1 - 2\cos\omega_r T_s) + \sin\omega_r T_s}\right|. \tag{13}$$

From (11) to (13), it can be found that the stability conditions for $K_{\rm ph}$ are different in three cases. Case II is even opposite to Case III. Therefore, the controller parameters must be designed according to the work region of the system. In fact, the grid impedance exists and varies with load. The inherent resonance frequency f_r will decrease due to the inductive grid impedance, and the work region might change from one to another. The previous design for $K_{\rm ph}$ may not meet the new stability condition, which may potentially result in the system instability. In view of this, Case I is the safest work region, but the constraint $f_r < f_s/6$ needs to be achieved at the expense of increasing the *LCL*-filter cost.

IV. Proposed Delay-Compensation Control Link

From Section III, it can be found that due to the system delays, $f_s/6$ becomes a critical resonance frequency for the proportional inverter-side current feedback, and three work regions are divided. Case I is the safest work region, however, with a strict constraint $f_r < f_s/6$. If the critical resonance frequency is extended, a wider region of Case I can be obtained, and the system will be robust to grid impedance. Therefore, a delay-compensation control link is proposed to replace the proportional part of the PR fundamental current controller and widen the critical resonance frequency, which can be expressed as

$$G_{\rm cf}(z) = \frac{K_{\rm pf} z}{1 + z}. \tag{14}$$

Fig. 4 shows the z-domain model of dual-loop current method with the delay-compensation control link, where the resonant part of $G_{\rm cf}(z)$ is still ignored for simplicity.

With the proposed delay-compensation control link, the open-loop transfer function of grid current loop $T_d(z)$ can be derived from Fig. 4 as (15) shown at the bottom of this page.

Similar to Section III, in order to ensure that no open-loop unstable poles exist in $T_d(z)$, the judging criterion for $K_{\rm pf}$ is

$$T_d(z) = G_{\rm ch}(z) K_{\rm pwm} \cdot \frac{(1+z)\left[\omega_r T_s(z^2 - 2z\cos\omega_r T_s + 1) - \sin\omega_r T_s (z-1)^2\right]}{(L_1 + L_2)\omega_r z\,(1+z)\,(z-1)(z^2 - 2z\cos\omega_r T_s + 1) + K_{\rm pwm} K_{pf} z[\omega_r T_s(z^2 - 2z\cos\omega_r T_s + 1) + \frac{L_2}{L_1}\sin\omega_r T_s (z-1)^2]} \tag{15}$$

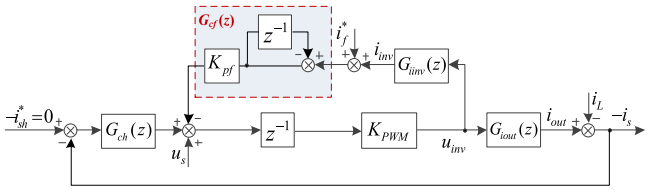

Fig. 4. z-domain model of dual-loop current control method with the delay-compensation control link.

derived in Appendix B and can be expressed as

$$0 < K_{\rm pf} < \min\left(K_d', K_d'', K_d'''\right) \text{ and } f_r \in \left(0, \frac{f_s}{4}\right) \tag{16}$$

where K_d', K_d'', K_d''' are defined as (17) shown at the bottom of this page.

According to (16), four cases are divided to further illustrate the system stability as follows:

Case A: $f_r < f_s/6$ and $0 < K_{\rm pf} < \min(K_d', K_d'', K_d''')$.

Case B: $f_s/6 < f_r < f_s/4$ and $0 < K_{\rm pf} < \min(K_d', K_d'', K_d''')$.

Case C: $f_s/6 < f_r < f_s/4$ and $K_{\rm pf} > \min(K_d', K_d'', K_d''')$.

Case D: $f_r > f_s/4$ and $K_{\rm pf} > 0$.

In Case A, the parameters in Table I are adopted with the inherent resonance frequency $f_{r2} = 2.03$ kHz, and the range of (16) is $0 < K_{\rm pf} < 2.38\,\Omega$. $K_{\rm pf} = 1.51\,\Omega$ is chosen for Case A. In Case B and Case C, the parameters are adopted with the resonance frequency $f_{r1} = 3.08$ kHz, and the range of (16) is $0 < K_{\rm pf} < 1.92\,\Omega$. Hence, $K_{\rm pf} = 1.38\,\Omega$ is chosen for Case B, while $K_{\rm pf} = 2.3\,\Omega$ is chosen for Case C. In Case D, the *LCL* filter parameters are $L_1 = 100\,\mu$H, $L_2 = 50\,\mu$H, and $C_f = 50\,\mu$f with the inherent resonance frequency $f_{r3} = 3.90$ kHz. In this case, no $K_{\rm pf}$ exists to meet (16), and $K_{\rm pf} = 1.51\,\Omega$ is chosen. Fig. 5 shows the Bode diagrams of $T_d(z)$ in four cases, where $G_{\rm ch}(z) = 1\,\Omega$.

From Fig. 5, it can be seen that in Case A and Case B, the phase plots of $T_d(z)$ only cross over $-180°$ at the crossing-over frequency f_c, which is less than the actual resonance frequency f_r'. In Case C and Case D, the phase plots of $T_d(z)$ cross over $-180°$ twice at the crossing-over frequency f_c and the actual resonance frequency f_r'. According to the Nyquist stability criterion [25],

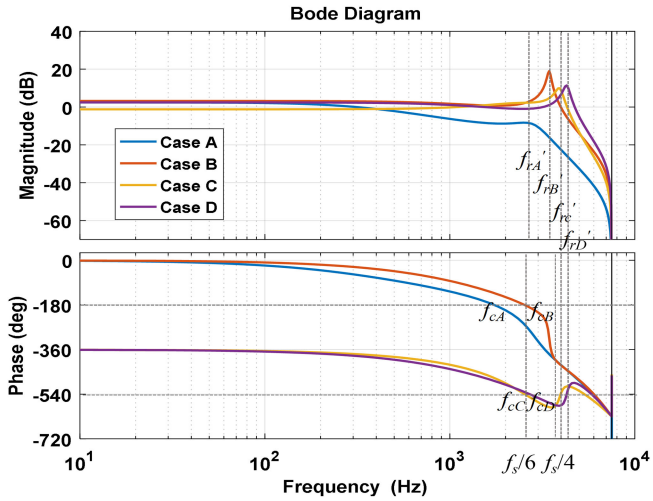

Fig. 5. Bode diagrams of $T_d(z)$ in four cases with $G_{\rm ch}(z) = 1\,\Omega$.

[32], the stability conditions with the delay-compensation control link can be summarized as follows:

Case A ($f_r < f_s/6$ and $0 < K_{pf} < min\,(K_d', K_d'', K_d'''))$ and Case B ($f_s/6 < f_r < f_s/4$ and $0 < K_{pf} < min\,(K_d', K_d'', K_d'''))$: No open-loop unstable poles exist, and the phase plots of $T_d(z)$ cross over $-180°$ only at f_c in the direction of phase falling. In order to make the system stable, the gain of $T_d(z)$ at f_c must be less than 0 dB. Hence, the corresponding stability condition can be expressed as

$$\left|T_d\left(z = e^{j\omega_c T_s}\right)\right| < 1. \tag{18}$$

Case C ($f_s/6 < f_r < f_s/4$ and $K_{pf} > min\,(K_d', K_d'', K_d'''))$ and Case D ($f_r > f_s/4$ and $K_{pf} > 0$): A pair of open-loop unstable poles occur, and the phase plots of $T_d(z)$ cross over $-180°$ at both f_c and f_r' in the direction of phase falling and phase rising, respectively. To make the system stable, the gain of $T_d(z)$ at f_c must be less than 0 dB and the gain at f_r' must be greater than 0 dB. As a result, the stability condition can be expressed as

$$\left|T_d\left(z = e^{j\omega_c T_s}\right)\right| < 1 \text{ and } \left|T_d\left(z = e^{j\omega'_r T_s}\right)\right| > 1. \tag{19}$$

$$\begin{cases} K_d' \triangleq \dfrac{2(L_1+L_2)\omega_r\,(1+\cos\omega_r T_s)}{K_{\rm pwm}\omega_r T_s\,(1+\cos\omega_r T_s) + 2K_{\rm pwm}\frac{L_2}{L_1}\sin\omega_r T_s} \\ \quad = \dfrac{2(L_1+L_2)\omega_r}{K_{\rm pwm}\omega_r T_s + 2K_{\rm pwm}\frac{L_2}{L_1}\tan(0.5\omega_r T_s)} \\ K_d'' \triangleq \dfrac{2(L_1+L_2) + 4(L_1+L_2)\frac{1}{T_s}\frac{L_2}{\omega_r L_1}\tan 0.5\omega_r T_s\left(1-\tan^2 0.5\omega_r T_s\right)}{K_{\rm pwm}T_s + 4K_{\rm pwm}\frac{L_2}{\omega_r L_1}\tan 0.5\omega_r T_s + 4K_{\rm pwm}\frac{1}{T_s}\left(\frac{L_2}{\omega_r L_1}\right)^2\tan^2 0.5\omega_r T_s} \\ K_d''' \triangleq \dfrac{2(L_1+L_2)\omega_r\cos\omega_r T_s}{K_{\rm pwm}\omega_r T_s\,\cos\omega_r T_s + K_{\rm pwm}\frac{L_2}{L_1}\sin\omega_r T_s} \\ \quad = \dfrac{2(L_1+L_2)\omega_r}{K_{\rm pwm}\omega_r T_s + K_{\rm pwm}\frac{L_2}{L_1}\tan\omega_r T_s} \end{cases} \tag{17}$$

As previously mentioned, it can be seen that if the judging criterion in (16) is satisfied, the control system is located in one work region as Case B, and the stability condition will be consistent when $f_r < f_s/6$ and $f_s/6 < f_r < f_s/4$. Therefore, with the proposed delay-compensation control link instead of proportional control link, the valid damping region of inverter-side current feedback has been successfully extended from (0, $f_s/6$) to (0, $f_s/4$).

V. Current Controller Parameter Design Criterion

The damping property and harmonic compensation accuracy are the main concerns of APFs, and proper current controller parameters must be designed to obtain satisfactory performances. In this section, a systematic controller parameter criterion is studied. In particular, a numerical optimization algorithm is developed to obtain optimal damping property, and a design method based on root locus plot and Bode diagram is presented to achieve high harmonic compensation accuracy.

A. Numerical Optimization Algorithm for Optimal Damping Property

An optimization target should be defined in a numerical optimization algorithm. Normally, the damping ratio ζ_i of the system pole is chosen as an evaluation index of damping property [33], which can be calculated in z-domain by

$$\zeta_i = -\cos\left(\angle\left(\frac{1}{T_s}\ln z_i\right)\right) \tag{20}$$

where $\angle$ denotes the angle of the complex number, and z_i denotes the closed-loop pole of APF control system, i.e., the pole of $T_d(z)/[1+T_d(z)]$.

For convenient implementation in MATLAB, $1-\zeta_i$ is adopted. In fact, maximizing the damping ratio ζ_i of the pole is equivalent to minimizing the corresponding $1-\zeta_i$. Since the damping ratios of all system poles should be maximized in the optimization process, the pole with the lowest damping ratio is only considered for simplicity. As a result, the optimization target of the proposed algorithm is to minimize the following expression:

$$F = \min_{K_{\rm pf},K_{\rm ph}}\left(\max_i(1-\zeta_i)\right) \tag{21}$$

where the proportional gains of current controllers $K_{\rm pf}$ and $K_{\rm ph}$ are the variables to optimize. The closed-loop poles introduced by the resonant controller units are not considered, because they have limited influences on the resonance poles and vary little with $K_{\rm pf}$ and $K_{\rm ph}$.

A function *fmin-search* is used in MATLAB to implement the damping optimization. For the APF system with the inherent resonance frequency $f_{r1} = 3.08$ kHz, the optimization results are $K_{\rm pf} = 1.63\,\Omega$, $K_{\rm ph} = 0.397\,\Omega$, $F = 0.755$, and $\zeta_i = 0.245$.

B. A Design Method Based on Root Locus Plot and Bode Diagram

In the fundamental and harmonic current controllers, the resonant controller (R) unit is widely adopted to eliminate the steady-state error at the fundamental or harmonic frequency, which is defined as

$$G_{\rm rn}(s) = K_{\rm rn}\cdot\frac{s\cos\left(\phi_n^*\right)-\omega_n\sin\left(\phi_n^*\right)}{s^2+(\omega_n)^2} \tag{22}$$

where K_{rn} is the resonant gain of the R unit for the harmonic order n. ϕ_n^* and ω_n are the compensation angle and the resonant angular frequency of that R unit, respectively. In particular, $n=1$ refers to the fundamental frequency. Applying the prewarped Tustin transformation to (22), an equivalent z-domain transfer function is obtained as (23) shown at the bottom of this page.

First, the parameters of the fundamental current controller $G_{\rm cf}(z)$ are designed, because the fundamental current loop is considered as the inner loop of grid current loop. Neglecting little phase delay at the fundamental angular frequency ω_1, the fundamental compensation angle ϕ_1^* is set to 0. Hence, the open-loop transfer function of the fundamental current loop can be expressed as

$$\begin{aligned}T_f(z) &= \underbrace{\left[\frac{K_{\rm pf}z}{1+z}+K_{r1}\frac{\omega_1\tan(0.5\omega_1T_s)\left(z^2-1\right)}{{\omega_1}^2(z-1)^2+{\omega_1}^2\tan^2(0.5\omega_1T_s)(z+1)^2}\right]}_{G_{\rm cf}(z)}\\ &\cdot\left[\frac{K_{\rm pwm}\omega_rT_s(z^2-2z\cos\omega_rT_s+1)+K_{\rm pwm}\frac{L_2}{L_1}\sin\omega_rT_s(z-1)^2}{(L_1+L_2)\omega_rz(z-1)(z^2-2z\cos\omega_rT_s+1)}\right].\end{aligned} \tag{24}$$

Due to the existence of $K_{\rm pf}z/(1+z)$, the root locus of (24) with K_{r1} variation cannot be plotted. To solve this issue, an equivalent characteristic equation can be derived from (24) as

$$1+K_{r1}\cdot\left[\frac{\omega_1\tan(0.5\omega_1T_s)\left(z^2-1\right)}{\omega_1^2(z-1)^2+\omega_1^2\tan^2(0.5\omega_1T_s)(z+1)^2}\cdot\frac{(1+z)\cdot G_{\rm plant}(z)}{(1+z)+K_{pf}z\cdot G_{\rm plant}(z)}\right]=0 \tag{25}$$

where K_{r1} becomes an equivalent proportional coefficient.

Fig. 6(a) plots the root locus of (25), where the stable range of the fundamental resonant gain is $0 < K_{\rm r1} < 3.95\times 103\ \Omega\cdot$rad/s. Fig. 6(b) shows the open-loop Bode diagrams of the fundamental current loop under three stable K_{r1}. Constrained by the IEEE harmonic current limit standard [34], the open-loop gain of the fundamental current loop should be higher

$$G_{\rm rn}(z) = K_{\rm rn}\frac{\omega_n\tan(0.5\omega_nT_s)\cos\left(\phi_n^*\right)\left(z^2-1\right)-\omega_n\sin\left(\phi_n^*\right)\tan^2(0.5\omega_nT_s)(z+1)^2}{\omega_n^2(z-1)^2+\omega_n^2\tan^2(0.5\omega_nT_s)(z+1)^2} \tag{23}$$

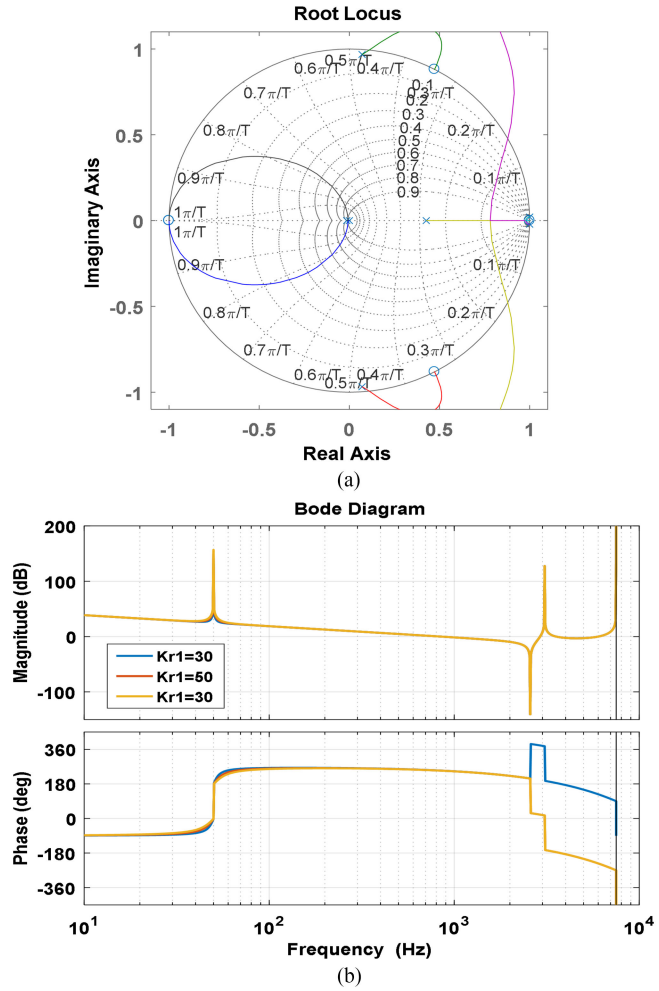

Fig. 6. Design of the fundamental resonant gain K_{r1}. (a) Root locus plot. (b) Open-loop Bode diagrams of fundamental current loop under three stable K_{r1}.

than 40 dB at the fundamental angular frequency ω_1. Therefore, $K_{\mathrm{r1}} = 50\ \Omega{\cdot}\mathrm{rad/s}$ is chosen to meet the gain requirement.

Then, the parameters of the harmonic current controller $G_{\mathrm{ch}}(z)$ are designed. Considering that load curent i_L mainly contains $(6k \pm 1)$th $(k = 0,\ 1,\ 2\ldots)$ harmonic components [9], a series of paralleled resonant units tuning at these harmonic frequencies are required in $G_{\mathrm{ch}}(z)$. Hence, the z-domain transfer function of harmonic current controller can be expressed as (26) shown at the bottom of the page, where $\omega_n = n\omega_1$ and $n = 6k\ \pm 1$. In this paper, the maximum harmonic compensation order is the 25th and hence, $k \in [1, 2, 3, 4]$.

In (26), ϕ_n^* is designed to compensate the phase delay at the harmonic frequency. Besides, ϕ_n^* should be less than 90° to avoid the resonance trap effect introduced by $G_{\mathrm{ch}}(z)$. Thus, the compensation angle of the nth resonant unit is selected as

$$\phi_n^* = \left|\angle G_{\mathrm{plant\_}h}\left(z = e^{j\omega_n T_s}\right)\right| \text{ and } \phi_n^* < 90^\circ \tag{27}$$

where $G_{\mathrm{plant\_}f}(z)$ is the transfer function of control plant of grid current loop, which can be expressed as

$$G_{\mathrm{plant\_}h}(z) = \frac{K_{\mathrm{pwm}} G_{i\mathrm{out}}(z)}{z + zT_f(z)}. \tag{28}$$

In (26), the resonant gain K_{rn} is designed in the increasing order of harmonic frequency. Take the fifth resonant unit as example. Assuming that the harmonic current controller is only comprised of a proportional part K_{ph} and the fifth resonant unit, an equivalent characteristic equation of grid current loop can be expressed as

$$1 + K_{r5} \cdot \left[\frac{\cos(\phi_5^*)\tan(0.5\omega_5 T_s)(z^2-1) - \sin(\phi_5^*)\tan^2(0.5\omega_5 T_s)(z+1)^2}{\omega_5(z-1)^2 + \omega_5\tan^2(0.5\omega_5 T_s)(z+1)^2} \cdot \frac{G_{\mathrm{plant\_}h}(z)}{1 + K_{\mathrm{ph}} \cdot G_{\mathrm{plant\_}h}(z)}\right] = 0. \tag{29}$$

Fig. 7(a) plots the root locus of (29), where the stable range of the fifth resonant gain is $0 < K_{r5} < 6.63 \times 103\ \Omega{\cdot}\mathrm{rad/s}$. Fig. 7(b) shows the open-loop Bode diagrams of grid current loop under three stable K_{r5}. Restricted by the IEEE harmonic current limit standard [34], the open-loop gain of grid current loop should be higher than 46 dB at the fifth harmonic frequency. Therefore, $K_{\mathrm{r5}} = 100\ \Omega{\cdot}\mathrm{rad/s}$ is chosen to satisfy the gain requirement.

For other resonant units, the resonant gain K_{rn} can be designed similar to K_{r5}. During the design process, the harmonic current controller $G_{\mathrm{ch}}(z)$ is comprised of a proportional part K_{ph} and the determined resonant units. An equivalent characteristic equation is then derived in which K_{rn} serves as the proportional coefficient. Finally, a suitable resonant gain K_{rn} is selected according to the corresponding root locus plot and Bode diagrams.

Table II lists the controller parameters of the dual-loop current control method with the assumption of $L_g = 0$, and the system stability is examined when L_g varies up to 10% p.u. (1.53 mH), which corresponds to a short-circuit ratio of 10 [35]. Fig. 8 shows the closed-loop pole maps of the APF control system when L_s varies up to 10% p.u. (the closed-loop poles introduced by the R units are not displayed since they vary little inside the unit circle). The proportional control link and the delay-compensation control link are adopted in the fundamental current controller. In Fig. 8(a), the proportional control link is adopted with $K_{\mathrm{pf}} = 0.8\ \Omega$ and $K_{\mathrm{ph}} = 0.7\ \Omega$, which meets the stability condition $0.399\ \Omega < K_{\mathrm{ph}} < 0.796\ \Omega$ by (13). In Fig. 8(b), the delay-compensation control link is adopted with controller parameters in Table II, which meets $0 < K_{\mathrm{ph}} < 0.787\ \Omega$ by (18).

$$G_{\mathrm{ch}}(z) = K_{\mathrm{ph}} + \sum_{n=6k\pm1} K_{\mathrm{rn}} \frac{\omega_n \tan(0.5\omega_n T_s)\cos\left(\phi_n^*\right)\left(z^2-1\right) - \omega_n \sin\left(\phi_n^*\right)\tan^2(0.5\omega_n T_s)(z+1)^2}{\omega_n^2(z-1)^2 + \tan^2(0.5\omega_n T_s)\omega_n^2(z+1)^2} \tag{26}$$

TABLE II
CONTROLLER PARAMETERS OF DUAL-LOOP CURRENT CONTROL METHOD WITH ASSUMPTION OF $L_g = 0$

Controller	Parameter			
Fundamental current controller G_{cf}	$K_{pf} = 1.63\ \Omega$		$K_{r1} = 50\ \Omega$·rad/s	
Harmonic current controller G_{ch}	$K_{ph} = 0.397\ \Omega$			
	$K_{r5} = 100\ \Omega$·rad/s	$\phi_5^* = 17°$	$K_{r7} = 100\ \Omega$·rad/s	$\phi_7^* = 26°$
	$K_{r11} = 100\ \Omega$·rad/s	$\phi_{11}^* = 42°$	$K_{r13} = 100\ \Omega$·rad/s	$\phi_{13}^* = 50°$
	$K_{r17} = 50\ \Omega$·rad/s	$\phi_{17}^* = 65°$	$K_{r19} = 50\ \Omega$·rad/s	$\phi_{19}^* = 73°$
	$K_{r23} = 50\ \Omega$·rad/s	$\phi_{23}^* = 88°$	$K_{r25} = 50\ \Omega$·rad/s	$\phi_{25}^* = 89°$
DC-side voltage controller PI	$K_p = 0.4\ \Omega$		$K_I = 0.002\ \Omega$·rad/s	

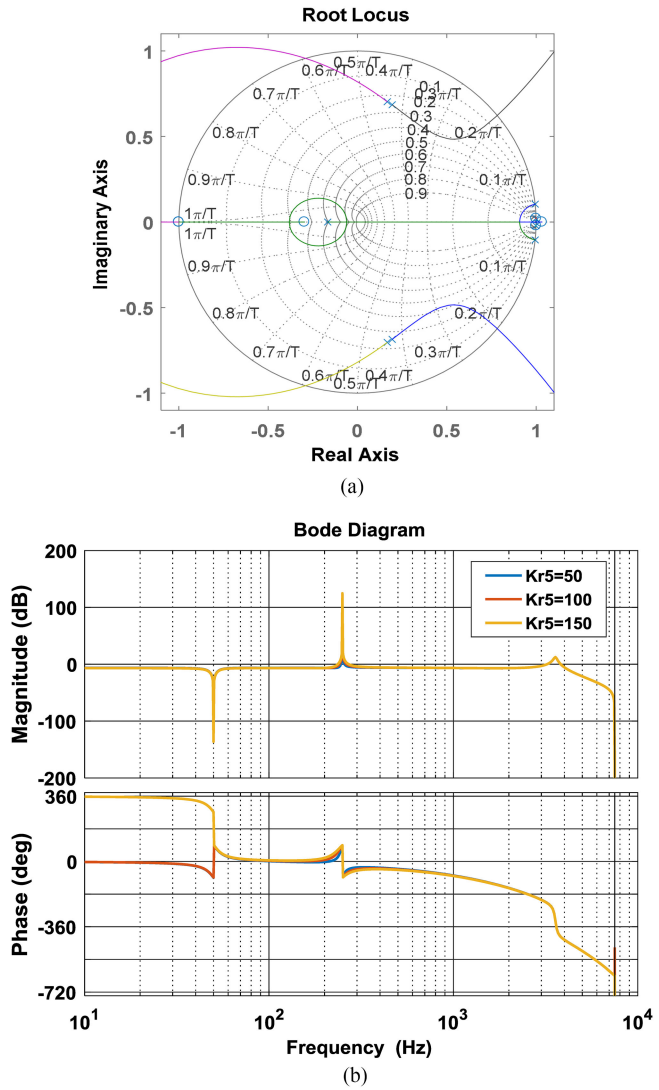

Fig. 7. Design of the fifth resonant gain K_{r5}. (a) Root locus plot. (b) Open-loop Bode diagrams of grid current loop under three stable K_{r5}.

From Fig. 8(a), the resonance poles move outside the unit circle for 40 μH $< L_s <$ 1.53 mH, which corresponds to 1.84 kHz $< f_r <$ 2.58 kHz. In comparison, the resonance poles in Fig. 8(b) are always inside the unit circle. Note that the resonance poles in Fig. 8(a) vary little for 200 μH $< L_s <$ 1.53 mH. Thereinto, $L_s = 280\ \mu$H is chosen to depict the worst stability condition,

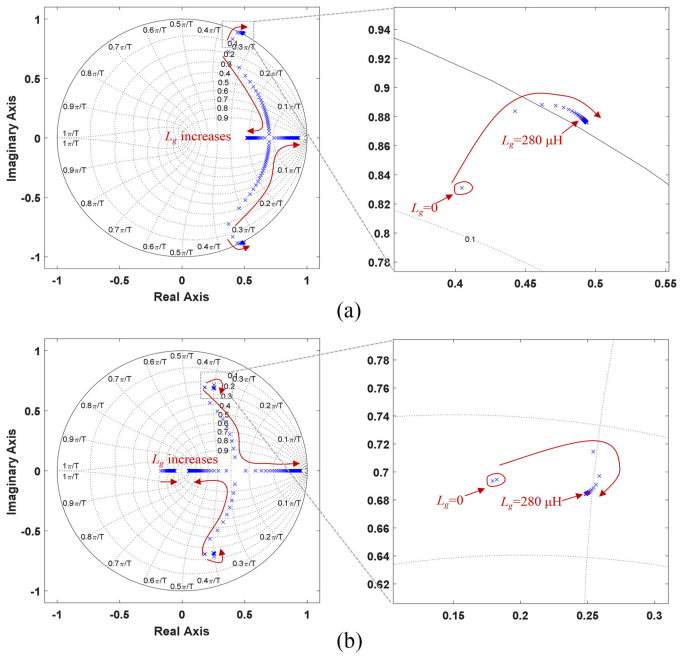

Fig. 8. Closed-loop pole maps of the APF control system when L_s varies up to 0.1 p.u. (1.53 mH). (a) With the proportional control link. (b) With the delay-compensation control link.

since its resonance poles are almost farthest outside the unit circle.

VI. EXPERIMENTAL RESULTS

A 30 kVA *LCL*-type shunt APF prototype is built based on a TMS320F28335 DSP, whose main parameters have been listed in Table I. Two sets of experiments are conducted to verify the stability conditions of dual-loop current control method and the improved robustness with the delay-compensation control link. The experimental prototype is shown in Fig. 9, where a Fluke F435 power quality analyzer and a YOKOGAWA DL850 oscilloscope are used for capturing the experimental results.

Fig. 10 shows the waveforms of grid current i_s and its harmonic spectrum with the nonlinear RL load before the operation of shunt APF. The grid current i_s contains rich harmonic components with a total harmonic distortion (THD) up to 24.7%. The harmonic currents are of $(6k \pm 1)$th (e.g., 5th, 7th, 11th, 13th . . .) order frequencies.

Fig. 9. 30 kVA *LCL*-type shunt APF prototype in the experiments.

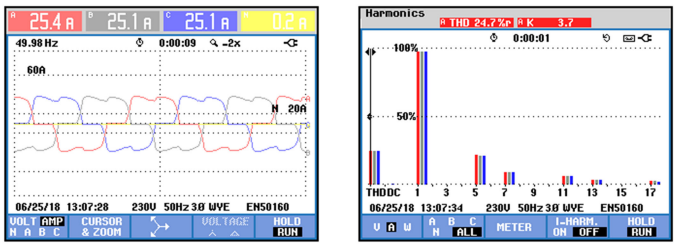

(a) (b)

Fig. 10. Waveforms of grid current i_s without APF. (a) Phase currents. (b) Harmonic spectrum.

A. Verifying the Stability Conditions of Dual-Loop Current Control Method

To verify the stability conditions of dual-loop current control method in Section IV, experiments are conducted with $L_s = 0$ and four groups of controller parameters. Two groups of controller parameters are designed by (18) to examine the stability condition of Case B, while the other two groups are designed by (19) to examine the stability condition of Case C.

Fig. 11 presents the steady-state experimental waveforms of grid current with $K_{\rm pf} = 1.38\,\Omega$, which is lower than $\min(K_d', K_d'', K_d''')$, i.e, 1.917 Ω. According to (18), the stability condition of Case B is calculated as $0 < K_{\rm ph} < 0.785\,\Omega$. $K_{\rm ph} = 0.5\,\Omega$ is chosen for Fig. 11(a), while $K_{\rm ph} = 1.3\,\Omega$ is chosen for Fig. 11(b) (other controller parameters are designed similarly to Section V). As seen in Fig. 11(a), the harmonics of grid current are effectively eliminated with its THD reduced from 24.7% to 4.5%. Comparatively, in Fig. 11(b), the APF system tends to be unstable, and the grid current shows serious high-frequency oscillation with its THD only reduced to 9.8%.

Fig. 12 presents the transient experimental waveforms with $0 < K_{\rm pf} < \min(K_d', K_d'', K_d''')$ when load increases, in which u_s is the Phase-A grid voltage at the PCC, i_s is the Phase-A grid current, and $i_{\rm out}$ is the Phase-A output current of APF. Meanwhile, Fig. 13 gives the corresponding spectrum of APF output current $i_{\rm out}$. As seen from Figs. 12(a) and 13(a), the APF system keeps stable and eliminates grid harmonics effectively under step load. Nevertheless, in Figs. 12(b) and 13(b), the APF output current $i_{\rm out}$ shows harsh high-frequency resonance, and the actual resonance frequency locates near 2.13 kHz.

Fig. 14 presents the steady-state waveforms of grid current i_s with $K_{\rm pf} = 2.45\,\Omega$, which is greater than $\min(K_d', K_d'', K_d''')$, i.e., 1.917 Ω. According to (19), the stability condition of Case C is calculated as $0.589\,\Omega < K_{\rm ph} < 0.769\,\Omega$. $K_{\rm ph} = 0.7\,\Omega$ is chosen for Fig. 14(a), while $K_{\rm ph} = 0.3\,\Omega$ is chosen for Fig. 14(b) (other controller parameters are designed similar to Section V). It can be seen from Fig. 14(a) that a good steady-state compensation result is obtained for grid current i_s with a THD of 4.8%. In comparison, the grid current i_s in Fig. 11(b) shows high-frequency oscillation with a high THD of 9.5%.

Fig. 15 presents the transient experimental waveforms with $K_{\rm pf} > \min(K_d', K_d'', K_d''')$ when load increases, and Fig. 16 gives the corresponding spectrum of APF output current $i_{\rm out}$. From Figs. 15(a) and 16(a), it can be seen that the APF output current $i_{\rm out}$ is able to eliminate grid harmonics effectively under step load. However, in Figs. 15(b) and 16(b), severe resonance currents occur near 4.08 kHz, which worsens the harmonic compensation performances.

Figs. 11–16 prove that the proposed dual-loop current control method can obtain good steady-state and transient compensation performances if the controller parameters meet the stability conditions. Otherwise, serious high-frequency resonance may occur due to a weak damping property. Besides, the APF system is also unstable when $K_{\rm pf} > \min(K_d', K_d'', K_d''')$ and $|T_d(z = e^{{\rm j}\omega_c T_s})| > 1$, which can refer to the case with $0 < K_{\rm pf} < \min(K_d', K_d'', K_d''')$ and $|T_d(z = e^{{\rm j}\omega_c T_s})| > 1$.

B. Verifying the Improved Robustness With the Delay-Compensation Control Link

To show the superior robustness of the proposed delay-compensation control link, an inductor $L_s = 280\,\mu$H is inserted in series with the grid at PCC to emulate the inductive grid impedance. The proportional control link and the delay-compensation control link are adopted in the fundamental current controller, and experiments are done under both $L_s = 0$ and $L_s = 280\,\mu$H.

Fig. 17 presents the steady-state waveforms of grid current i_s with two control links when $L_s = 0$. In this case, the inherent resonance frequency f_r (3.08 kHz) is located within the range $(f_s/6, f_s/4)$. The controller parameters with the proportional control link are $K_{\rm pf} = 0.8\,\Omega$ and $K_{\rm ph} = 0.7\,\Omega$, which meets the stability condition of Case III, i.e., $0.399\,\Omega < K_{\rm ph} < 0.796\,\Omega$ by (13). The current controllers with the delay-compensation control link takes the parameters listed in Table II. As seen from Fig. 17, the THD of grid current i_s is 4.9% with the proportional control link, whereas the THD is further decreased to 3.9% with the delay-compensation control link. Fig. 18 shows the transient experimental waveforms with two control links when $L_s = 0$. As shown, both the control links obtain good transient

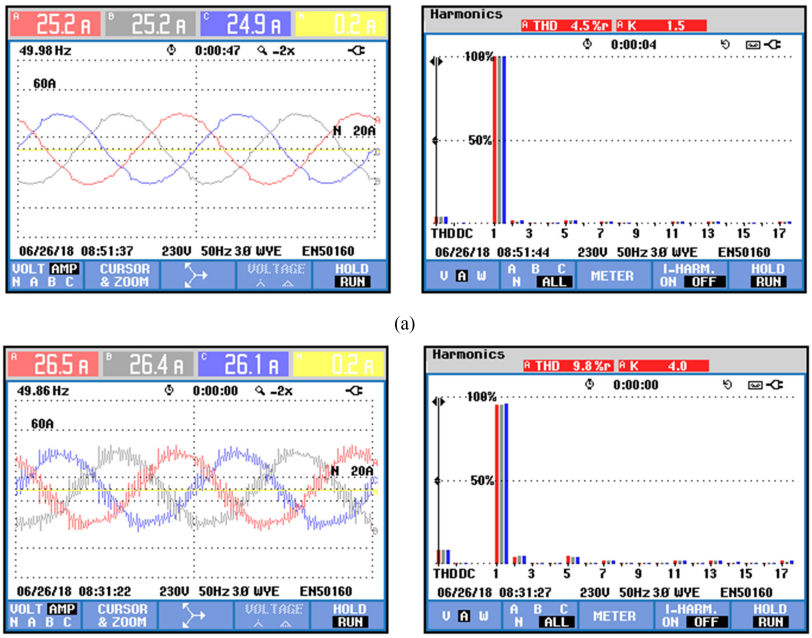

(a)

(b)

Fig. 11. Steady-state waveforms of grid current i_s with $0 < K_{\rm pf} < \min(K_d', K_d'', K_d''')$. (a) $|T_d(z = e^{j\omega cT_S})| < 1$. (b) $|T_d(z = e^{j\omega cT_S})| > 1$.

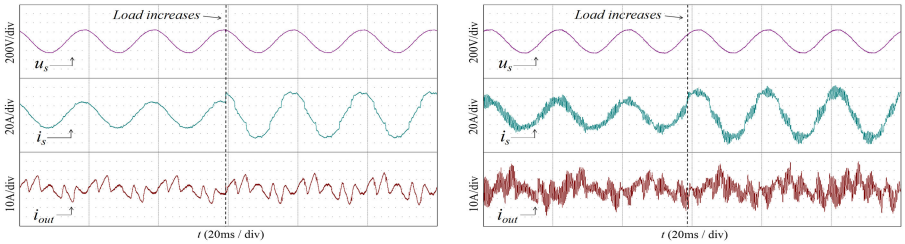

(a) (b)

Fig. 12. Transient experimental waveforms with $0 < K_{\rm pf} < \min(K_d', K_d'', K_d''')$. (a) $|T_d(z = e^{j\omega cT_S})| < 1$. (b) $|T_d(z = e^{j\omega cT_S})| > 1$.

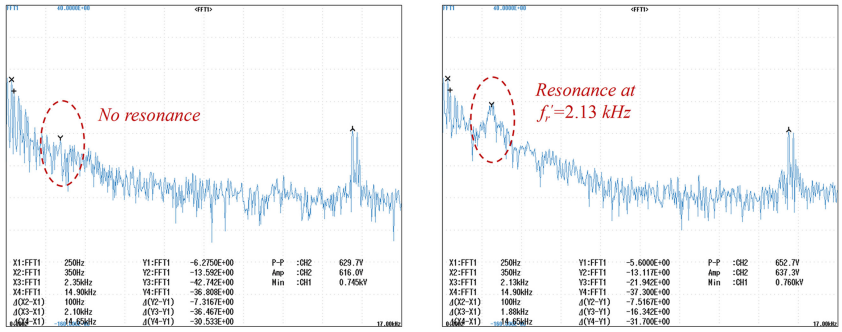

(a) (b)

Fig. 13. Spectrum of APF output current $i_{\rm out}$ with $0 < K_{\rm pf} < \min(K_d', K_d'', K_d''')$. (a) $|T_d(z = e^{j\omega cT_S})| < 1$. (b) $|T_d(z = e^{j\omega cT_S})| > 1$.

compensation results under step load (the spectrum of APF output current $i_{\rm out}$ is thus not given).

Fig. 19 presents the steady-state waveforms of grid current i_s with two control links when $L_s = 280\,\mu$H. In this case, the inherent resonance frequency f_r (2.03 kHz) is lower than $f_s/6$ (2.5 kHz). According to (12), the new stability condition with the proportional control link is $0.937\,\Omega < K_{\rm ph} < 2.65\,\Omega$, which $K_{\rm ph} = 0.7\,\Omega$ does not meet. In Fig. 19(a), high-frequency oscillation exists in grid current i_s with a high THD of 10.9%. Comparatively, in Fig. 19(b), the satisfactory steady-state compensation result is still obtained, and the THD of grid current is kept at a very low level of 4.1%.

Fig. 20 presents the transient experimental waveforms with two control links when $L_s = 280\ \mu$H, and Fig. 21 shows

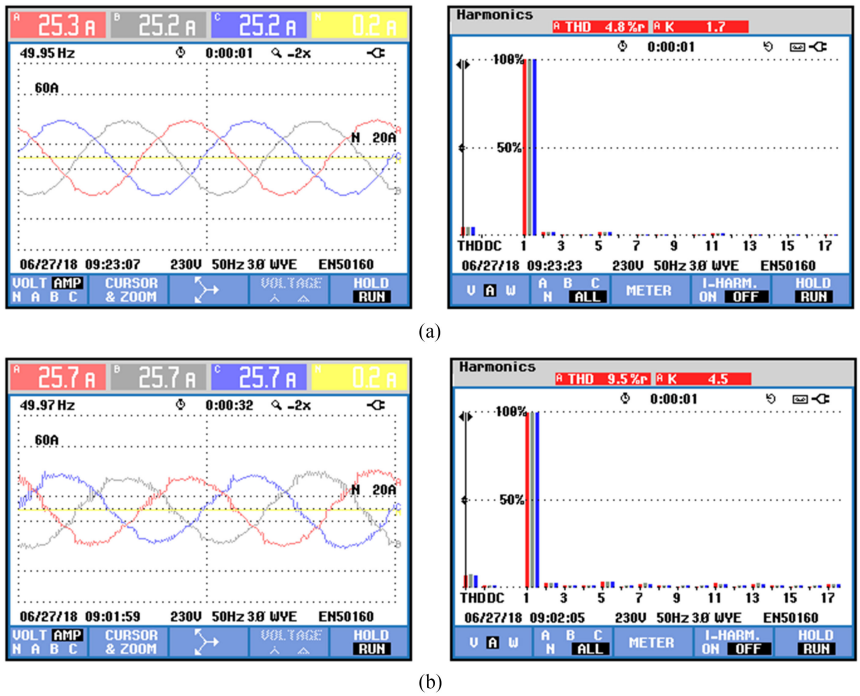

Fig. 14. Steady-state waveforms of grid current i_s with $K_{\rm pf} > \min(K_d', K_d'', K_d''')$. (a) $|T_d(z = e^{j\omega cT_s})| < 1$ and $|T_d(z = e^{j\omega r' T_s})| > 1$. (b) $|T_d(z = e^{j\omega r' T_s})| < 1$.

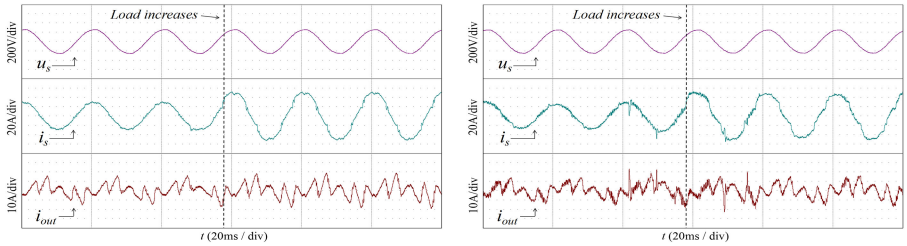

Fig. 15. Transient experimental waveforms with $K_{\rm pf} > \min(K_d', K_d'', K_d''')$. (a) $|T_d(z = e^{j\omega cT_s})| < 1$ and $|T_d(z = e^{j\omega r' T_s})| > 1$. (b) $|T_d(z = e^{j\omega r' T_s})| < 1$.

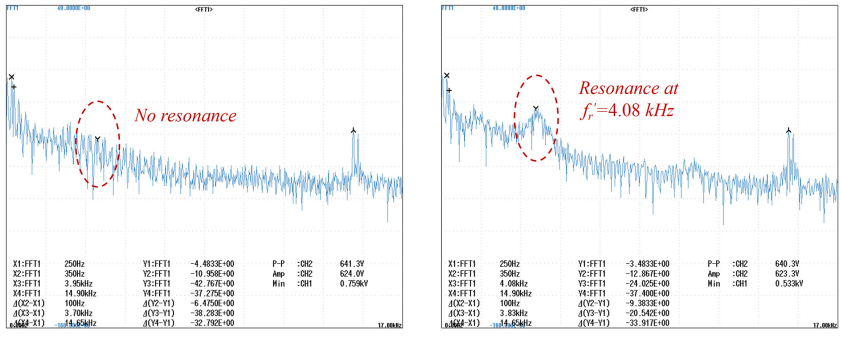

Fig. 16. Spectrum of APF output current $i_{\rm out}$ with $K_{\rm pf} > \min(K_d', K_d'', K_d''')$. (a) $|T_d(z = e^{j\omega cT_s})| < 1$ and $|T_d(z = e^{j\omega r' T_s})| > 1$. (b) $|T_d(z = e^{j\omega r' T_s})| < 1$.

the corresponding spectrum of APF output current $i_{\rm out}$. From Figs. 20(a) and 21(a), there is obvious resonance existing in the APF output current $i_{\rm out}$, and the actual resonance frequency locates near 2.53 kHz. Besides, the grid voltage u_s also shows high-frequency oscillation due to the inserted inductor. However, the delay-compensation control link still keeps a good transient compensation performance without resonance under step load in Figs. 20(b) and 21(b).

From Figs. 17–21, it can be found that the valid damping region of inverter-side current feedback is successfully extended to $(0, f_s/4)$ with the delay-compensation control link instead of the proportional control link. Meanwhile, the most

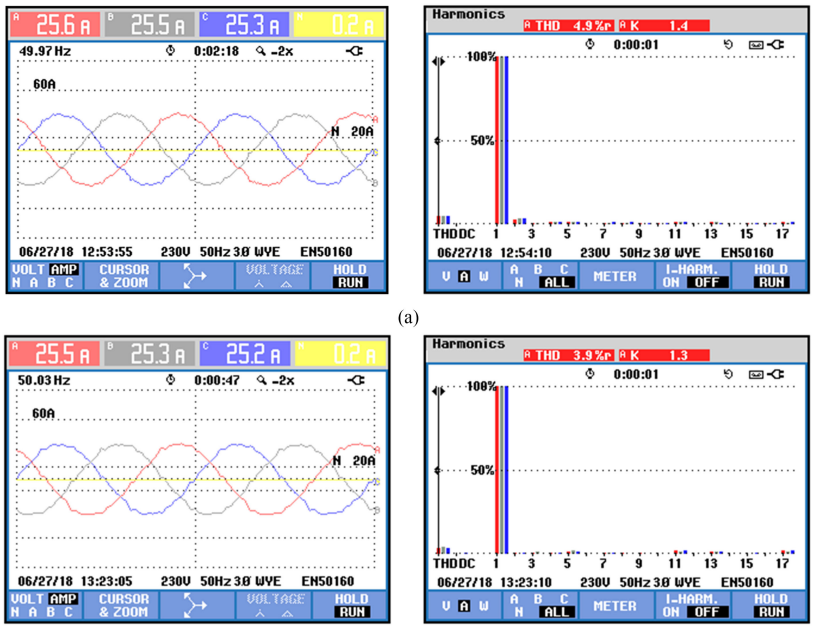

(a)

(b)

Fig. 17. Steady-state waveforms of grid current i_s when $L_s = 0$. (a) With the proportional control link. (b) With the delay-compensation control link.

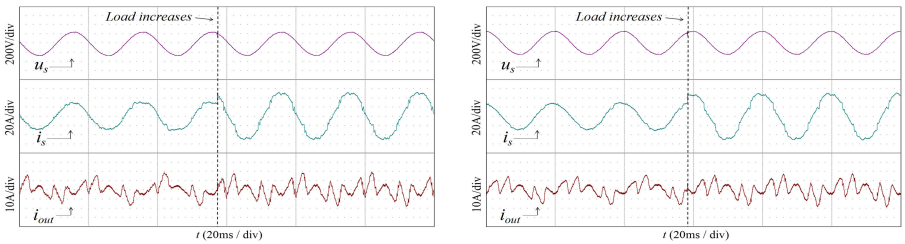

(a) (b)

Fig. 18. Transient experimental waveforms when $L_s = 0$. (a) With the proportional control link. (b) With the delay-compensation control link.

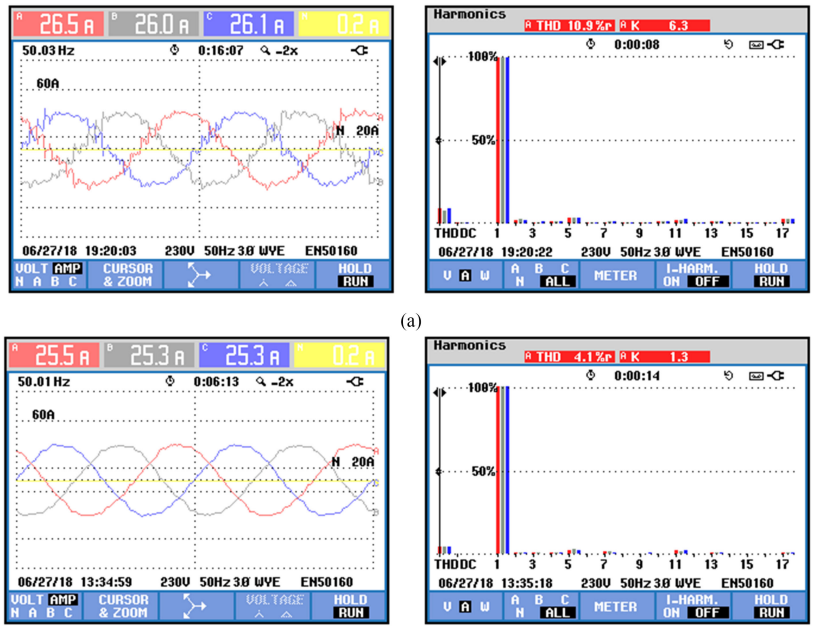

(a)

(b)

Fig. 19. Steady-state waveforms of grid current i_s when $L_s = 280\ \mu$H. (a) With the proportional control link. (b) With the delay-compensation control link.

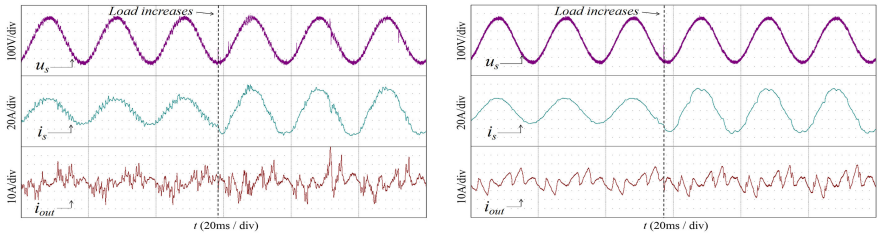

Fig. 20. Transient experimental waveforms when $L_s = 280\ \mu$H. (a) With the proportional control link. (b) With the delay-compensation control link.

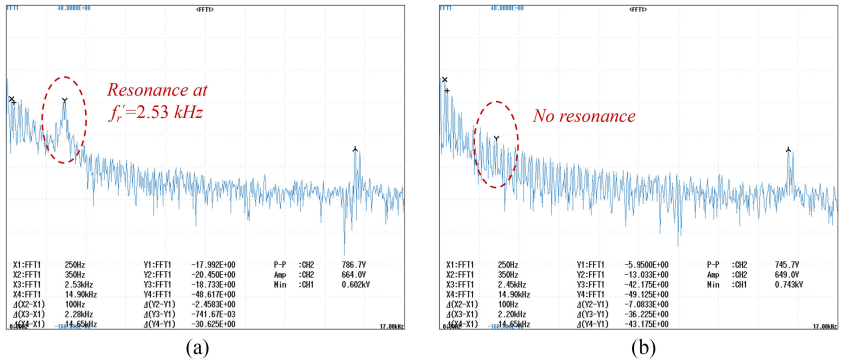

Fig. 21. Spectrum of APF output current i_{out} when $L_s = 280\ \mu$H. (a) With the proportional control link. (b) With the delay-compensation control link.

satisfactory steady-state and transient compensation performances are obtained with the controller parameters in Table II, which has validated the feasibility of the proposed parameter design criterion.

VII. Conclusion

This paper investigates a dual-loop current control method for digitally controlled *LCL*-type shunt APFs, and finds that the proportional inverter-side current feedback actually exists in the control loop when a PR unit is adopted as the fundamental current controller. Considering the delay effect, the valid damping region of proportional feedback is only up to one-sixth of the sampling frequency ($f_s/6$), which results in less robustness to the grid impedance. To address this issue, this paper proposes a delay-compensation control link to replace the proportional part of the PR fundamental controller and widen the damping region. Theoretical analysis proves that a wider damping region of $(0, f_s/4)$ is obtained, and hence, the system robustness is improved without adding extra sensors or introducing an extra active damping loop. Moreover, a systematic controller parameter design criterion is studied. In particular, a numerical optimization algorithm is developed to optimize damping property, and a design method based on root locus plot and Bode diagram is presented to enhance harmonic compensation accuracy. The experimental results are finally presented, which have verified the effectiveness of the proposed current controller and parameter design criterion.

Appendix A

First, considering that the harmonic current controller $G_{ch}(z)$ does not introduce unstable poles, the open-loop unstable poles of $T_p(z)$ in (6) are decided by the roots of

$$\begin{aligned}&(L_1+L_2)\omega_r z(z-1)(z^2-2z\cos\omega_r T_s+1)\\&\quad+K_{\rm pwm}K_{\rm pf}[\omega_r T_s(z^2-2z\cos\omega_r T_s+1)\\&\quad+\frac{L_2}{L_1}\sin\omega_r T_s(z-1)^2]=0.\end{aligned}\tag{A1.1}$$

To obtain the root positions, we take the w transform $z = (1+w)/(1-w)$ to equivalently transform the area outside the unit circle in the z-plane into the right-half plane in the w-plane [24]. In this way, (A1.1) can be changed as

$$a_0w^4+a_1w^3+a_2w^2+a_3w+a_4=0\tag{A1.2}$$

where

$$\begin{cases}a_0=4(L_1+L_2)\omega_r(1+\cos\omega_r T_s)\\\quad+2K_{\rm pf}K_{\rm pwm}\omega_r T_s(1+\cos\omega_r T_s)\\\quad+4K_{\rm pf}K_{\rm pwm}\dfrac{L_1}{L_2}\sin\omega_r T_s\\a_1=4(L_1+L_2)\omega_r(1+\cos\omega_r T_s)\\\quad-4K_{\rm pf}K_{\rm pwm}\omega_r T_s(1+\cos\omega_r T_s)\\\quad-8K_{\rm pf}K_{\rm pwm}\dfrac{L_1}{L_2}\sin\omega_r T_s\\a_2=4(L_1+L_2)\omega_r(1-\cos\omega_r T_s)\\\quad+4K_{\rm pf}K_{\rm pwm}\omega_r T_s\\\quad+4K_{\rm pf}K_{\rm pwm}\dfrac{L_1}{L_2}\sin\omega_r T_s\\a_3=4(L_1+L_2)\omega_r(1-\cos\omega_r T_s)\\\quad-4K_{\rm pf}K_{\rm pwm}\omega_r T_s(1-\cos\omega_r T_s)\\a_4=2K_{\rm pf}K_{\rm pwm}\omega_r T_s(1-\cos\omega_r T_s).\end{cases}\tag{A1.3}$$

According to Routh's method, the Routh array of the characteristic equation (A1.2) is

$$\begin{array}{lll} w^4: & a_0 & a_2 \quad a_4 \\ w^3: & a_1 & a_3 \quad 0 \\ w^2: & \dfrac{a_1a_2 - a_0a_3}{a_1} & a_4 \\ w^1: & \dfrac{a_3(a_1a_2 - a_0a_3) - a_1^2a_4}{a_1a_2 - a_0a_3} & \\ w^0: & a_4. & \end{array} \tag{A1.4}$$

In the *LCL* filter design, the resonance frequency f_r is usually less than one half of the switching frequency ($f_{sw}/2$) to ensure the effective attenuation of the switching harmonics [6], [26], i.e., $f_r < f_{sw}/2$. In this paper, $f_s = f_{sw}$ and hence the possible range of f_r is $(0, f_s/2)$. For $0 < f_r < f_s/2$, $a_0 > 0$. To avoid the right-half-plane roots for (A1.2), i.e., the open-loop unstable poles of $T_p(z)$, the conditions of coefficients in (A1.4) must satisfy

$$\begin{aligned} & a_1 > 0 \ \text{ and } \ \frac{a_1a_2 - a_0a_3}{a_1} > 0 \\ & \text{and } \ \frac{a_3(a_1a_2 - a_0a_3) - a_1^2a_4}{a_1a_2 - a_0a_3} > 0. \end{aligned} \tag{A1.5}$$

Then, the judging criteria for K_{pf}, which can ensure no open-loop unstable poles in $T_p(z)$, can be obtained as

$$\begin{cases} (1)\ \ 0 < K_{pf} < \min\left(K', K'', K'''\right) \quad \text{when } f_r \in \left(0, \dfrac{f_s}{6}\right) \\ \qquad \text{or when } f_r \in \left(\dfrac{f_s}{6}, \dfrac{f_s}{2}\right) \text{ and } \omega_r T_s(1 - 2\cos\omega_r T_s) \\ \qquad -\dfrac{L_2}{L_1}\sin\omega_r T_s < 0 \\ (2)\ \ \max\left(0, K'''\right) < K_{pf} < \min\left(K', K''\right) \\ \qquad \text{when } f_r \in \left(\dfrac{f_s}{6}, \dfrac{f_s}{2}\right) \text{ and } \omega_r T_s(1 - 2\cos\omega_r T_s) \\ \qquad -\dfrac{L_2}{L_1}\sin\omega_r T_s > 0 \end{cases} \tag{A1.6}$$

where K', K'', and K''' have been given in (8).

Note that in (A1.6), two judging criteria for K_{pf} are given when f_r is located in different frequency ranges of $(0, f_s/2)$. Combining (A1.6) and (8), the judging criteria, when $f_s/6 < f_r < f_s/2$, are analyzed as follows. First, when $f_r > f_s/6$ and $\omega_r T_s(1 - 2\cos\omega_r T_s) - L_2/L_1\sin\omega_r T_s < 0$, $K''' < 0$, then the inequality $0 < K_{pf} < \min(K', K'', K''')$ is invalid. Second, when $f_r > f_s/6$ and $\omega_r T_s(1 - 2\cos\omega_r T_s) - L_2/L_1\sin\omega_r T_s > 0$, $K' > 0$ and $K''' > 0$. In this case, the denominator of K''' is obviously less than that of K', while the numerators of K' and K''' are both the same $(L_1 + L_2)\omega_r$. Hence, $K''' > K'$ and the inequality $\max(0, K''') < K_{pf} < \min(K', K'')$ cannot be satisfied. To sum up, it can be found that when $f_s/6 < f_r < f_s/2$, the inequalities in (A1.6) are always invalid, and a pair of open-loop unstable poles always exist in $T_p(z)$. In addition, a pair of open-loop unstable poles will also occur in $T_p(z)$ when $f_r < f_s/6$ and $K_{pf} > \min(K', K'', K''')$ As mentioned above, the judging criterion for K_{pf} to ensure no open-loop unstable poles in $T_p(z)$ can be finally simplified as (7).

Appendix B

Considering that the harmonic current controller $G_{ch}(z)$ does not introduce unstable poles and the open-loop pole $z = 0$ is located inside the unit circle, the pole condition of $T_d(z)$ in (15) is decided by the roots of

$$\begin{aligned} & (L_1 + L_2)\omega_r(1 + z)(z - 1)(z^2 - 2z\cos\omega_r T_s + 1) \\ & \quad + K_{pwm}K_{pf}[\omega_r T_s(z^2 - 2z\cos\omega_r T_s + 1) \\ & \quad + \frac{L_2}{L_1}\sin\omega_r T_s(z - 1)^2] = 0. \end{aligned} \tag{A2.1}$$

Substituting $z = (1 + w)/(1 - w)$ into (A2.1), an equivalent characteristic equation can be derived as

$$a_0w^4 + a_1w^3 + a_2w^2 + a_3w + a_4 = 0 \tag{A2.2}$$

where

$$\begin{cases} a_0 = 2K_{pwm}K_{pf}\omega_r T_s(1 + \cos\omega_r T_s) + 4K_{pwm}K_{pf}\dfrac{L_2}{L_1}\sin\omega_r T_s \\ a_1 = 8(L_1 + L_2)\omega_r\ (1 + \cos\omega_r T_s) \\ \qquad - 4K_{pwm}K_{pf}\omega_r T_s(1 + \cos\omega_r T_s) \\ \qquad - 8K_{pwm}K_{pf}\dfrac{L_2}{L_1}\sin\omega_r T_s \\ a_2 = 4K_{pwm}K_{pf}\omega_r T_s + 4K_{pwm}K_{pf}\dfrac{L_2}{L_1}\sin\omega_r T_s \\ a_3 = 8(L_1 + L_2)\omega_r\ (1 - \cos\omega_r T_s) \\ \qquad - 4K_{pwm}K_{pf}\omega_r T_s(1 - \cos\omega_r T_s) \\ a_4 = 2K_{pwm}K_{pf}\omega_r T_s(1 - \cos\omega_r T_s). \end{cases} \tag{A2.3}$$

According to Routh's method, the Routh array of the characteristic equation (A2.2) is

$$\begin{array}{lll} w^4: & a_0 & a_2 \quad a_4 \\ w^3: & a_1 & a_3 \quad 0 \\ w^2: & \dfrac{a_1a_2 - a_0a_3}{a_1} & a_4 \\ w^1: & \dfrac{a_3(a_1a_2 - a_0a_3) - a_1^2a_4}{a_1a_2 - a_0a_3} & \\ w^0: & a_4. & \end{array} \tag{A2.4}$$

For $0 < f_r < f_s/2$, $a_0 > 0$. To avoid the right-half-plane roots for (A2.2), i.e., the open-loop unstable poles of $T_d(z)$, the conditions of coefficients in (A2.4) must meet

$$a_1 > 0 \ \ \& \ \ \frac{a_1a_2 - a_0a_3}{a_1} > 0 \ \ \& \ \ \frac{a_3(a_1a_2 - a_0a_3) - a_1^2a_4}{a_1a_2 - a_0a_3} > 0. \tag{A2.5}$$

From (A2.5), the judging criteria for $K_{\rm pf}$ to ensure no open-loop unstable poles in $T_d(z)$ can be derived as

$$\begin{cases} (1)\ \ 0 < K_{\rm pf} < \min\left(K_d', K_d'', K_d'''\right) \quad \text{when } f_r \in \left(0, \dfrac{f_s}{4}\right) \\ \qquad \text{or when } f_r \in \left(\dfrac{f_s}{4}, \dfrac{f_s}{2}\right) \text{ and } \omega_r T_s \cos \omega_r T_s \\ \qquad + \dfrac{L_2}{L_1} \sin \omega_r T_s > 0 \\ (2)\ \ \max\left(0, K_d'''\right) < K_{\rm pf} < \min\left(K_d', K_d''\right) \\ \qquad \text{when } f_r \in \left(\dfrac{f_s}{4}, \dfrac{f_s}{2}\right) \text{ and } \omega_r T_s \cos \omega_r T_s \\ \qquad + \dfrac{L_2}{L_1} \sin \omega_r T_s < 0 \end{cases} \tag{A2.6}$$

where K_d', K_d'', and K_d''' have been given in (17).

From (A2.6), it can be found that the judging criteria for $K_{\rm pf}$ is different with f_r located in different frequency ranges of $(0, f_s/2)$. Thereinto, the judging criteria when $f_s/6 < f_r < f_s/2$ are further discussed as follows. First, when $f_s/4 < f_r < f_s/2$ and $\omega_r T_s \cos\omega_r T_s + L_2/L_1 \sin\omega_r T_s > 0, \pi/2 < \omega_r T_s < \pi$ and $K_d''' < 0$. Hence, in this case, the inequality $0 < K_{\rm pf} < \min(K_d', K_d'', K_d''')$ is invalid. Second, when $f_s/4 < f_r < f_s/2$ and $\omega_r T_s \cos\omega_r T_s + L_2/L_1 \sin\omega_r T_s < 0$, it can be obtained from (17) that $K_d' > 0, K_d''' > 0, 2\tan(0.5\omega_r T_s) > 0$ and $\tan(\omega_r T_s) < 0$. In this case, the denominator of K_d''' is less than that of K_d', while the numerators of K_d' and K_d''' are both the same $2(L_1 + L_2)\omega_r$. Hence, $K_d''' > K_d'$ and the inequality $\max(0, K_d''') < K_{pf} < \min(K_d', K_d'')$ is obviously invalid. As mentioned above, it has been found that when $f_s/4 < f_r < f_s/2$, the inequality in (A2.6) is always invalid and a pair of open-loop unstable poles always exists in $T_d(z)$. Besides, when $f_r < f_s/4$ and $K_{\rm pf} > \min(K_d', K_d'', K_d''')$, a pair of open-loop unstable poles will also occur in $T_d(z)$. Consequently, the judging criterion for $K_{\rm pf}$ to ensure no open-loop unstable poles in $T_d(z)$ can be rewritten as (16).

REFERENCES

[1] F. Blaabjerg, R. Teodorescu, M. Liserre, and A. V. Timbus, "Overview of control and grid synchronization for distributed power generation systems," *IEEE Trans. Ind. Electron.*, vol. 53, no. 5, pp. 1398–1409, Oct. 2006.

[2] Z. Zeng, H. Yang, S. Tang, and R. Zhao, "Objective-oriented power quality compensation of multi-functional grid-tied inverters and its application in micro-grids," *IEEE Trans. Power Electron.*, vol. 30, no. 3, pp. 1255–1265, Mar. 2015.

[3] D. J. Hogan, F. J. Gonzalez-Espin, J. G. Hayes, G. Lightbody, and R. Foley, "An adaptive digital-control scheme for improved active power filtering under distorted grid conditions," *IEEE Trans. Ind. Electron.*, vol. 65, no. 2, pp. 988–999, Jul. 2018.

[4] F. Briz, P. García, M. W. Degner, D. Díaz-Reigosa, and J. M. Guerrero, "Dynamic behavior of current controllers for selective harmonic compensation in three-phase active power filters," *IEEE Trans. Ind. Appl.*, vol. 49, no. 3, pp. 1411–1420, May/Jun. 2013.

[5] M. Liserre, F. Blaabjerg, and S. Hansen, "Design and control of an *LCL* filter-based three-phase active rectifier," *IEEE Trans. Ind. Appl.*, vol. 41, no. 5, pp. 1281–1291, Sep./Oct. 2005.

[6] W. Wu, Y. He, and F. Blaabjerg, "An *LLCL* power filter for single-phase grid-tied inverter," *IEEE Trans. Power Electron.*, vol. 27, no. 2, pp. 782–789, Feb. 2012.

[7] W. Wu, Y. He, T. Tang, and F. Blaabjerg, "A new design method for the passive damped *LCL* and *LLCL* filter-based single-phase grid-tied inverter," *IEEE Trans. Ind. Electron.*, vol. 60, no. 10, pp. 4339–4350, Oct. 2013.

[8] J. He and Y. W. Li, "Generalized closed-loop control schemes with embedded virtual impedances for voltage source converters with LC or *LCL* filters," *IEEE Trans. Power Electron.*, vol. 27, no. 4, pp. 1850–1861, Apr. 2012.

[9] Y. Tang, P. C. Loh, P. Wang, F. H. Choo, F. Gao, and F. Blaabjerg, "Generalized design of high performance shunt active power filter with output *LCL* filter," *IEEE Trans. Ind. Electron.*, vol. 59, no. 3, pp. 1443–1452, Mar. 2012.

[10] F. Liu, Y. Zhou, S. Duan, J. Yin, B. Liu, and F. Liu, "Parameter design of a two-current-loop controller used in a grid-connected inverter system with *LCL* filter," *IEEE Trans. Ind. Electron.*, vol. 56, no. 11, pp. 4483–4491, Nov. 2009.

[11] I. J. Gabe, V. F. Montagner, and H. Pinheiro, "Design and implementation of a robust current controller for VSI connected to the grid through an *LCL*-filter," *IEEE Trans. Power Electron.*, vol. 24, no. 6, pp. 1444–1452, Jun. 2009.

[12] M. Malinowski and S. Bernet, "A simple voltage sensorless active damping scheme for three-phase PWM converters with an *LCL* filter," *IEEE Trans. Ind. Electron.*, vol. 55, no. 4, pp. 1876–1880, Apr. 2008.

[13] J. Xu, S. Xie, L. Huang, and L. Ji, "Design of *LCL*-filter considering the control impact for grid-connected inverter with one current feedback only," *IET. Power. Electron.*, vol. 10, no. 11, pp. 1324–1332, Jun. 2017.

[14] Y. Tang, P. C. Loh, P. Wang, F. H. Choo, and F. Gao, "Exploring inherent damping characteristic of *LCL*-filters for three-phase grid-connected voltage source inverters," *IEEE Trans. Power Electron.*, vol. 27, no. 3, pp. 1433–1443, Mar. 2012.

[15] W. Li, X. Ruan, D. Pan, and X. Wang, "Full-feedforward schemes of grid voltages for a three-phase *LCL*-type grid-connected inverter," *IEEE Trans. Ind. Electron.*, vol. 60, no. 6, pp. 2237–2250, Jun. 2013.

[16] V. Miskovic, V. Blasko, T. M. Jahns, A. H. C. Smith, and C. Romenesko, "Observer-based active damping of *LCL* resonance in grid-connected voltage source converters," *IEEE Trans. Ind. Appl.*, vol. 50, no. 6, pp. 3977–3985, Nov./Dec. 2014.

[17] J. Dannehl, F. W. Fuchs, S. Hansen, and P. B. Thøgersen, "Investigation of active damping approaches for PI-based current control of grid-connected pulse width modulation converters with *LCL* filters," *IEEE Trans. Ind. Appl.*, vol. 46, no. 4, pp. 1509–1517, Jul./Aug. 2010.

[18] J. Xu, S. Xie, and T. Tang, "Active damping-based control for grid-connected *LCL*-filter inverter with injected grid current feedback only," *IEEE Trans. Ind. Electron.*, vol. 61, no. 9, pp. 4746–4758, Sep. 2014.

[19] H. Yi, F. Zhuo, Y. Zhang, Y. Li, and W. Zhan, "A source current detected shunt active power filter control scheme based on vector resonant controller," *IEEE Trans. Ind. Appl.*, vol. 50, no. 3, pp. 1953–1965, May/Jun. 2014.

[20] C. Zou, B. Liu, S. Duan, and R. Li, "Influence of delay on system stability and delay optimization of grid-connected inverters with *LCL* filter," *IEEE Trans. Ind. Informat.*, vol. 10, no. 3, pp. 1775–1784, Aug. 2014.

[21] J. Wang, J. D. Yan, L. Jiang, and J. Zou, "Delay-dependent stability of single-loop controlled grid-connected inverters with *LCL* filters," *IEEE Trans. Power Electron.*, vol. 31, no. 1, pp. 743–757, Jan. 2016.

[22] D. Yang, X. Ruan, and H. Wu, "A real-time computation method with dual sampling mode to improve the current control performance of the *LCL*-type grid-connected inverter," *IEEE Trans. Ind. Electron.*, vol. 62, no. 7, pp. 4563–4572, Jul. 2015.

[23] L. Harnefors, X. Wang, A. G. Yepes, and F. Blaabjerg, "Passivity-based stability assessment of grid-connected VSCs—An overview," *IEEE J. Emerg. Sel. Topics Power Electron.*, vol. 4, no. 1, pp. 116–126, Mar. 2016.

[24] C. Bao, X. Ruan, X. Wang, W. Li, D. Pan, and K. Weng, "Design of injected grid current regulator and capacitor-current-feedback active- damping for *LCL*-type grid-connected inverter," in *Proc. IEEE Energy Conver. Congr. Expo.*, Sep. 2012, pp. 579–586.

[25] D. Pan, X. Ruan, C. Bao, W. Li, and X. Wang, "Capacitor-current-feedback active damping with reduced computation delay for improving robustness of *LCL*-type grid-connected inverter," *IEEE Trans. Power Electron.*, vol. 29, no. 7, pp. 3414–3427, Jul. 2014.

[26] X. Li, X. Wu, Y. Geng, X. Yuan, C. Xia, and X. Zhang, "Wide damping region for *LCL*-type grid-connected inverter with an improved capacitor-current-feedback method," *IEEE Trans. Power Electron.*, vol. 30, no. 9, pp. 5247–5258, Sep. 2015.

[27] Y. He, X. Wang, and X. Ruan, "Improve the robustness of digitally-controlled *LCL*-filtered inverters against grid impedance variation with a lag compensator," in *Proc. IEEE Energy Conver. Congr. Expo.*, 2017, pp. 76–82.

[28] Y. Tang, W. Yao, P. C. Loh, and F. Blaabjerg, "Design of *LCL* filters with LCL resonance frequencies beyond the Nyquist frequency for grid-connected converters," *IEEE J. Emerg. Sel. Topics Power Electron.*, vol. 4, no. 1, pp. 3–14, Mar. 2016.
[29] L. Harnefors, R. Finger, X. Wang, H. Bai, and F. Blaabjerg, "VSC input-admittance modeling and analysis above the Nyquist frequency for passivity-based stability assessment," *IEEE Trans. Ind. Electron.*, vol. 64, no. 8, pp. 6362–6370, Aug. 2017.
[30] M. Liserre, R. Teodorescu, and F. Blaabjerg, "Stability of photovoltaic and wind turbine grid-connected inverters for a large set of grid impedance values," *IEEE Trans. Power Electron.*, vol. 21, no. 1, pp. 263–272, Jan. 2006.
[31] S. G. Parker, B. P. McGrath, and D. G. Holmes, "Regions of active damping control for *LCL* filters," in *Proc. IEEE Energy Conver. Congr. Expo.*, 2012, pp. 53–60.
[32] G. C. Goodwin, S. F. Graebe, and M. E. Salgado, *Control System Design*. Upper Saddle River, NJ, USA: Prentice-Hall, 2000, pp. 136–140.
[33] M. Wagner, T. Barth, R. Alvarez, C. Ditmanson, and S. Bernet, "Discrete-time active damping of *LCL*-resonance by proportional capacitor current feedback," *IEEE Trans. Ind. Appl.*, vol. 50, no. 6, pp. 3977–3985, Nov./Dec. 2014.
[34] *IEEE recommended practice and requirements for harmonic control in electric power systems*, IEEE Standard 519, Jun. 2014, pp. 1–26.
[35] A. Etxegarai, P. Eguia, E. Torres, and E. Fernandez, "Impact of wind power in isolated power systems," in *Proc. IEEE Mediterranean Electrotechnical Conf.*, Mar. 2012, pp. 63–66.

Lei Yang was born in Henan, China, in 1993. He received the B.S. degree in electrical engineering from Zhejiang University, Hangzhou, China, in 2015. He is currently working toward the Ph.D. degree in control of active power filter at the College of Electrical Engineering, Zhejiang University.

His research interests include power quality, control technology, and renewable energy generation.

Jiaqiang Yang (M'11) was born in Jiangsu, China, in 1970. He received the Ph.D. degree in electrical engineering from Zhejiang University, Hangzhou, China, in 2004.

Since 2004, he worked as a Lecturer, Associate Professor, and Professor with the College of Electrical Engineering, Zhejiang University. From 2012 to 2013, he was a Research Fellow with the College of Electrical and Computer, National University of Singapore, Singapore. He is currently a Professor. His research interests include active power filters, flywheel energy storage systems, and the design and control of motor for electrical vehicles.